Journal of Catalysis **207,** 76–87 (2002)
doi:10.1006/jcat.2002.3508, available online at http://www.idealibrary.com on IDEAL®

Shape and Edge Sites Modifications of MoS_2 Catalytic Nanoparticles Induced by Working Conditions: A Theoretical Study

Hannes Schweiger,* Pascal Raybaud,*,[1] Georg Kresse,† and Hervé Toulhoat‡

*Division Chimie et Physico-chimie Appliquées, Département Thermodynamique et Modélisation Moléculaire, and ‡Direction Scientifique, Institut Français du Pétrole, 1-4 av. de Bois-Préau, BP311-92852 Rueil-Malmaison Cedex, France; and †Institut für Materialphysik and Center for Computational Materials Science, Universität Wien, Sensengasse 8, A-1090 Vienna, Austria

Received October 10, 2001; revised December 13, 2001; accepted December 13, 2001

Determination of the morphology and electronic properties of single-layer nanosize MoS_2 particles is of considerable interest for a better understanding of the active phase of hydrotreating catalysts. We propose an original approach, based on density functional calculations applied to various types of MoS_2 clusters containing up to 200 atoms, to evaluate accurately the surface energies of the Mo-edge and S-edge terminated surfaces. The results are expressed as a function of the chemical potential of sulfur, which is in turn controlled by the temperature and the ratio of partial pressures of H_2S and H_2. Gibbs–Curie–Wulff equilibrium morphologies reveal that a high chemical potential of sulfur leads to triangular-shaped particles terminated by the Mo-edge surface, giving an interpretation of the observations made recently by scanning tunneling microscopy (STM). Simulations of the STM images for the most stable clusters reveal a qualitatively good agreement with experiments. Moreover, our approach predicts that varying the potential of sulfur modifies the local Mo-edge structure and the shape of the nanoparticles. Finally, the thermodynamic diagram for a MoS_2 particle with a realistic size shows that the creation of one sulfur vacancy at the corner and on the edge is possible under HDS working conditions. © 2002 Elsevier Science (USA)

Key Words: **hydrodesulfurization; molybdenum disulfide; MoS_2 catalysts; surface properties; morphology; density functional theory (DFT); scanning tunneling microscopy (STM).**

I. INTRODUCTION

With the aim of meeting more and more severe environmental specifications on sulfur-containing fuels, research dedicated to hydrotreatment catalysis has been prompted to use many cutting-edge characterization techniques for a better understanding of the active phase of the industrial catalyst (2, 3). Transmission electron microscopy (4, 5), X-ray photoelectron spectroscopy (6–9), Mössbauer spectroscopy (10), laser Raman spectroscopy (5, 11), high-resolution electron microscopy (12), and extended X-ray absorption fine structure (EXAFS) (13–17) brought complementary insights for refining the physical characterization of the MoS_2- and Co (or Ni)-promoted active phases. To complement the experimental characterization, theoretical methods, such as density functional theory (DFT) calculations, have become increasingly popular for the study of MoS_2-based systems. Their advantage over experimental techniques is that they allow a direct microscopic description of the active site (18–21) and possibly a realistic atomistic modeling of the important processes involved in the hydrotreatment catalysis (22–27). Moreover, a combination of *ab initio* calculations with thermodynamic arguments opens a route to predict the morphology of nanosized particles (18, 28). It has been shown, for instance, how the sulfo-reductive environment, represented by the temperature- and pressure-dependent chemical potential of sulfur, influences the chemical composition of the MoS_2 active edges (18). At the same time scanning tunneling microscopy (STM) has been successfully applied by Helveg and coworkers (1, 29) to study the atomic-scale structure of gold-supported single-layer MoS_2 nanoclusters, revealing their shape and the edge structure. Together with EXAFS and DFT techniques, STM studies have contributed significantly to our knowledge about the active site.

It also confirms that morphological and structural effects have significance for the number of active sites in industrial catalysts, as suggested earlier by the geometrical model of Kasztelan and coworkers (30–32). Indeed, this model shows that it is possible to establish quantitative structure activity relationships between HDS activities and the number and type of active sites according to the shape of the catalyst particles (chain, triangles, hexagons). As a consequence, controlling MoS_2 morphologies means controlling the nature of the exposed active sites and, thus, the reactivity itself.

As suggested in Ref. (18), the equilibrium morphologies of single-layer MoS_2 particles can be determined by combining surface energies calculated by DFT and the Gibbs–Curie–Wulff construction (33, 34).

Straightforward slab calculations for single-layer MoS_2 sheets do, however, not allow determination of the surface

[1] To whom correspondence should be addressed. Fax: +33 1 47 52 70 58. E-mail: pascal.raybaud@ifp.fr.

0021-9517/02 $35.00

energy of the so-called Mo-edge or S-edge independently. To overcome this difficulty, it is necessary to simulate large triangular-shaped clusters exhibiting only one type of edge. This is exactly the major scope of the present work (Section IIB).

By combining the calculated surface energies with thermodynamic arguments we also derive the equilibrium morphology of single-layer MoS_2 nanosized particles under various environmental conditions (Section IIC). Simulated STM images are presented for the edge structures of MoS_2 clusters at various chemical potentials of sulfur and they are compared with the recent STM images (1) (Section IIIB). Finally, the energy for the creation of a sulfur vacancy is evaluated at the edge and on the corner of such particles (Section IIIC).

II. METHODS

A. DFT Calculations

The first-principles calculations presented here are based on density functional theory (see, e.g., Refs. (35–37)) and employ a plane-wave basis set (38, 39). To solve the Kohn Sham equations the Vienna *ab initio* simulation package (VASP) is used, which calculates the Kohn Sham ground state via an iterative unconstrained band-by-band matrix diagonalization scheme and an optimized charge-density mixing (40, 41). The electron–ion interaction is described by the projector augmented wave (PAW) method as proposed by Blöchl (42). Compared to conventional pseudopotentials (43, 44), this method has the advantage that the exact shape of the valence wavefunctions is taken into account, and this in turn can improve the description of transition metal compounds (45). A careful comparison of the relevant bulk and surface properties of MoS_2 revealed no significant differences between the present PAW calculations and the calculations based on the ultrasoft pseudopotentials employed in previous studies (18, 19, 25, 46). But since the PAW method allows for an exact description of the valence wavefunctions, describing also the exact nodal structure, we decided to use the more reliable PAW method for the present calculations. For the exchange-correlation functional, the local functional proposed by Perdew and Zunger (47) is used and corrected for nonlocal effects in the form of the generalized gradient approximation of Perdew and coworkers (48, 49). A plane-wave cutoff energy of 225 eV was used throughout this work.

The optimization of the atomic geometries is performed using a conjugate gradient minimization of the total energy, and by calculating the exact Hellman–Feynman forces acting on the ions in each optimization step. All atoms in the clusters were relaxed, but it was found that the relaxation affects mainly S adatoms and the first two layers of Mo and S atoms counted from the edges inward. Electronic relaxation was performed to an accuracy better than 1 meV/cell; the overall criterion was to minimize the forces acting on all ions to a value below 0.1 or 0.25 eV/Å, the latter value being used for the most unstable surface exhibiting highly undercoordinated Mo atoms. All calculations were carried out with Γ-point-only integration, which is justified by the use of large finite-size clusters. As a consequence, we estimate that the overall precision of the final surface energies is within 50 meV/atom.

B. Cluster Models

As was shown in Ref. (18), periodic calculations make it possible to determine the energetics and structure of the $(10\bar{1}0)$ surface, the so-called *Mo-edge*, and $(\bar{1}010)$ surface, the *S-edge*, under various chemical potentials of sulfur. However, these calculations had a significant and important shortcoming: they did not allow us to calculate the energy of the Mo-edge or S-edge *independently*. The reason for that is illustrated in Fig. 1. A single MoS_2 sheet cut along the dotted lines is terminated on one side by a Mo-edge and on the other side by a S-edge. It is not possible to change the type of edge by moving one of the straight dotted lines to a different cleavage plane. Therefore, slab calculations always yield the average surface energy of both types of edges.

Triangular-shaped clusters, however, offer a solution to this problem. The cluster on the left-hand side of Fig. 1, for instance, exhibits only S-edges, and the right-hand cluster only Mo-edges. We show in the next paragraph that the surface energy of both edges can be reliably calculated by varying the cluster size. Different terminations can be accounted for by simply terminating the clusters either with two S atoms per Mo, with a single S atom, or with a Mo atom. The relevant triangular clusters for the Mo-edge and the S-edge are presented in Figs. 2 and 3, respectively.

Both figures show results for triangles after full structural relaxation. In the following, we use the convention that 100

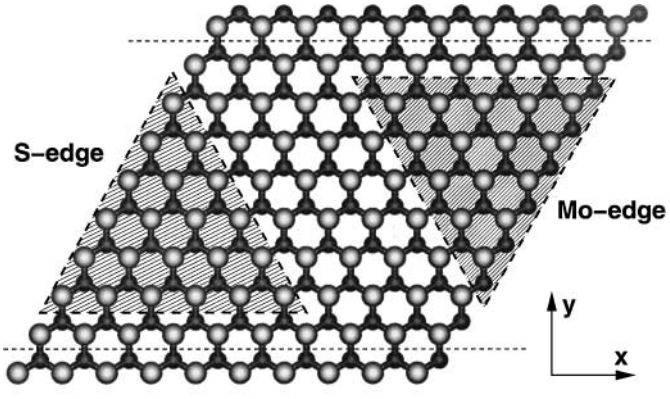

FIG. 1. Construction of triangular-shaped cluster models from the infinite MoS_2 slab (top view). Left-hand triangle, S-edge only; right-hand triangle, Mo-edge only; large grey balls, S atoms; small dark balls, Mo atoms.

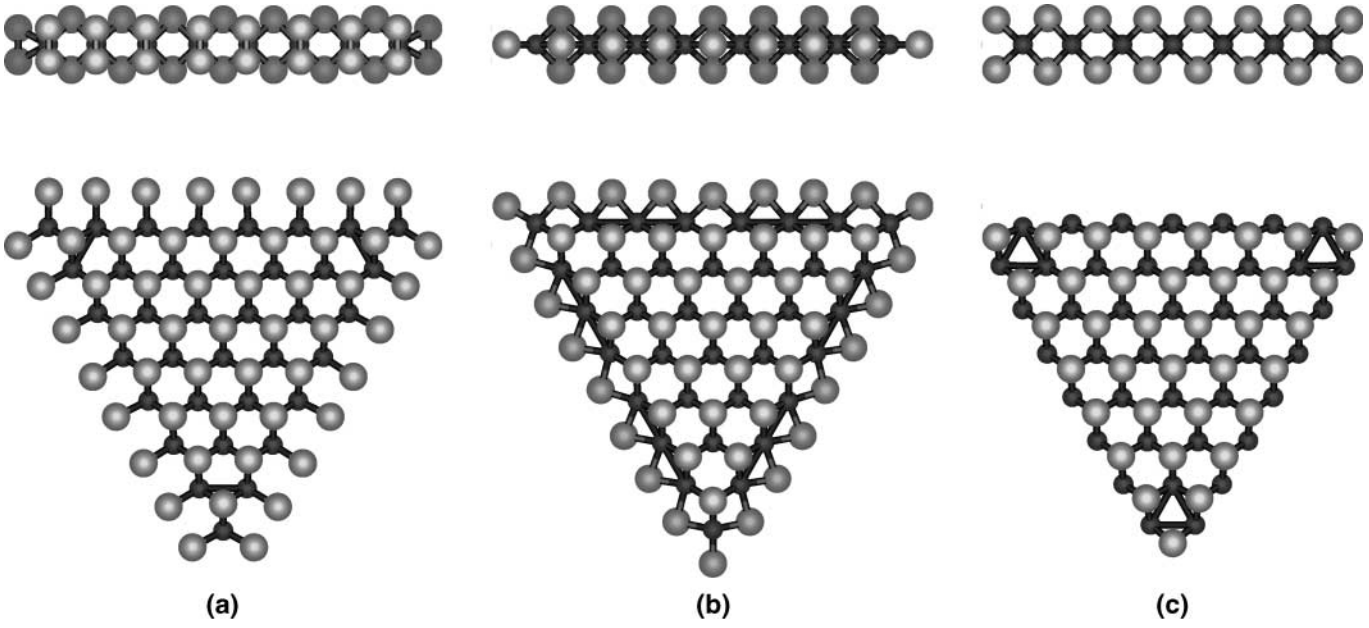

FIG. 2. Top view and side view of the triangular clusters terminated by the Mo-edge after relaxation. (a) 100% S coverage; (b) 50% S coverage; (c) 0% S coverage with capped corners. (Large grey balls, S atoms; small dark balls, Mo atoms.)

and 50% sulfur coverage correspond to two and one S atoms per Mo-edge atom, respectively, i.e., the percentage is referenced to the bulk terminated geometry. It is emphasized that the present study was on purpose restricted to sulfur coverage of 0, 50, and 100% for the Mo- and S-edges, since our previous slab calculations (18) indicate that only these coverages are thermodynamically stable.

In agreement with our previous study, the Mo-edge triangle with 100% sulfur coverage exhibits S_2 dimers after relaxation and the outer Mo atoms are sixfold coordinated (Fig. 2a). The Mo-edge with 50% sulfur coverage shows S monomers in a bridging position, and therefore the Mo atoms are sixfold coordinated again (see Fig. 2b). On the clean surface with 0% sulfur coverage, finally, the Mo atoms are fourfold coordinated, as depicted in Fig. 2c. In this case, we had to remove the Mo-corner atoms to be able to relax the model reliably.

For the S-edge with 100% sulfur coverage, the coordination of Mo atoms in the Mo–S outermost chain is six, and the sulfur atoms are in a bridge position close to their position in the bulk terminated case (Fig. 3a). Furthermore it should be noted that a slight pairing of the S_2 dimers is observed. Reducing the sulfur coverage to 50% leads to a *zigzag* configuration, as shown in (18) (see Fig. 3b). The S atoms do not lay perfectly in the same plane as the Mo atoms. The Mo atoms are only fourfold coordinated and the S monomers are again close to a bridge position. The S-edge with 0% sulfur is subjected to strong reconstructions due to the large undercoordination (twofold) of the Mo atoms, as depicted in Fig. 3c.

Furthermore, we varied the cluster size to check to what extent the local edge structure is influenced by the presence of corner sites and to ensure the convergence of surface energies, independent from the corner structure. In the following paragraphs, the cluster size is expressed by n, the number of Mo atoms per edge of the triangular cluster. For instance, for Figs. 2a and 2b, n is equal to 8. According to the type of cluster, n is allowed to vary between 4 and 11, implying that up to 200 atoms are included in the calculations.

C. Thermodynamics and Morphology Determination

In the same spirit as Ref. (18), the grand canonical potential, Ω, for a triangular MoS_2 nanocluster of size n, at a chemical potential of sulfur, μ_S, and molybdenum, μ_{Mo}, is defined as

$$\Omega(n, \mu_S) = E_{MoS_x} - \mu_{Mo} n_{Mo}^{tot} - \mu_S n_S^{tot}, \qquad [1]$$

where E_{MoS_x} is total energy of a triangular cluster of size n with a given type of edge and stoichiometry (as discussed in the previous paragraph), and n_S^{tot} and n_{Mo}^{tot} represent the total number of sulfur and molybdenum atoms, respectively. Using simple thermodynamics, as detailed in Ref. (18), chemical potential μ_S can be related to temperature T and partial sulfur pressure, p_{H_2S}, as

$$\mu_S - \mu_S^{bulk} = [h_{H_2S}(T) - h_{H_2}(T)] - E_S^{bulk} - T[s_{H_2S}(T) - s_{H_2}(T)] + RT \ln\left(\frac{p_{H_2S}}{p_{H_2}}\right), \qquad [2]$$

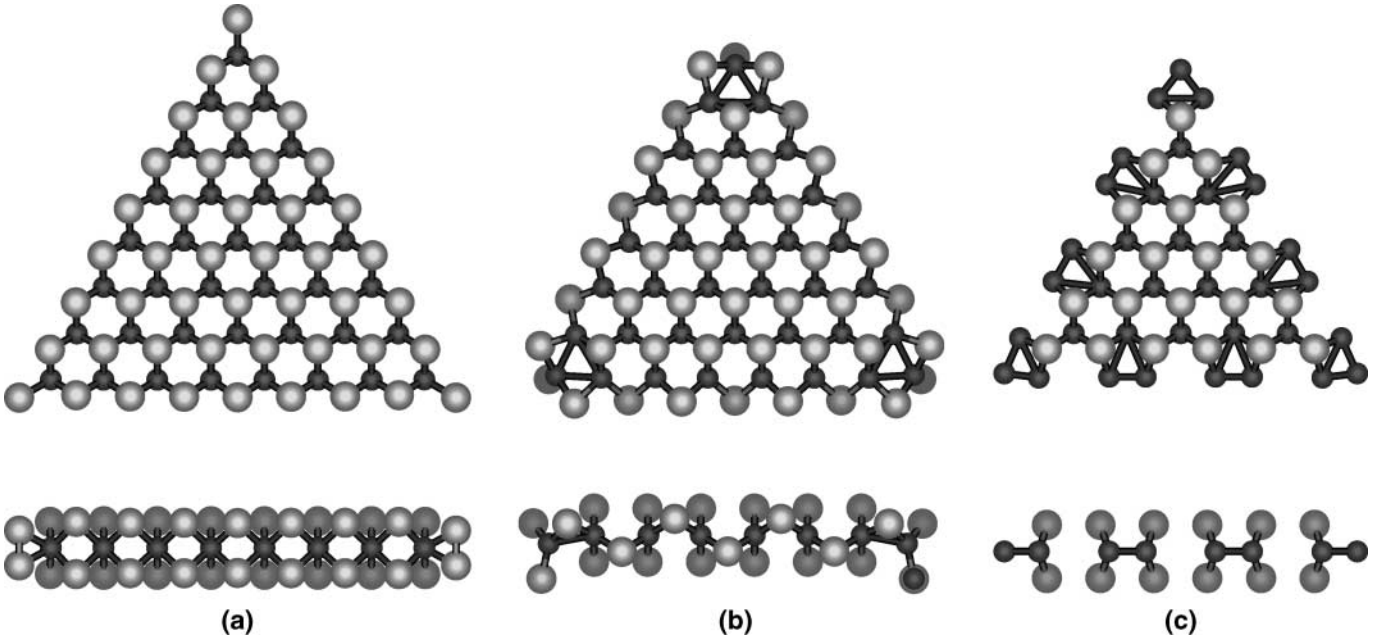

FIG. 3. Top view and side view of the triangular-shaped clusters terminated by the S-edge after relaxation. (a) 100% S coverage; (b) 50% S coverage; (c) 0% S coverage.

where h and s stand for enthalpies and entropies of H_2S or H_2.

Large values of μ_S correspond to sulfur-rich conditions, whereas small values of μ_S relate to strongly reducing conditions, where hydrogen is more abundant than H_2S in the gas phase. Our reference energies for sulfur are chosen such that the maximum chemical potential μ_S is zero, corresponding to conditions at which sulfur condenses as bulk S. The lower limit for μ_S is -1.30 eV. Below this limit, the gas phase is so strongly reducing that S prefers to be in the gas phase, and MoS_2 triangles are reduced to metallic body-centered cubic (bcc) Mo.

At thermal equilibrium, the chemical potentials of sulfur and molybdenum satisfy

$$2\mu_S + \mu_{Mo} \approx E^{ref}_{MoS_2}, \qquad [3]$$

where $E^{ref}_{MoS_2}$ is the total energy of an infinite MoS_2 monolayer per MoS_2 unit.

Combining Eqs. [1] and [3] yields

$$\Omega(n, \mu_S) = E_{MoS_x} - n^{tot}_{Mo} E^{ref}_{MoS_2} - \mu_S n_S, \qquad [4]$$

where

$$n_S = 2n^{tot}_{Mo} - n^{tot}_{S}, \qquad [5]$$

and where n_S stands for the excess or lack of sulfur atoms compared to the bulk stoichiometry. As shown in Tables 1 and 2, n_S depends on the cluster size, n, and can be positive or negative.

The reversible work for creating a small surface unit, dn, at constant μ is given by

$$d\Omega(\mu) = \sigma(\mu)\, dn, \qquad [6]$$

where $\sigma(\mu)$ is the surface energy per surface site for a given crystallographic orientation, corresponding to the Mo-edge, the S-edge, and the basal plane.

TABLE 1

Composition and Relevant Parameters of Triangular Mo-Edge Terminated Clusters as a Function of Sulfur Coverage and Size

S coverage	Size(n)	n_S	n^{tot}_{Mo}	n^{tot}_{S}	$\frac{n^{tot}_{S}}{n^{tot}_{Mo}}$	Δn_S
100%	4	16	10	36	3.60	$\frac{4}{3}$
	7	28	28	84	3.00	$\frac{4}{3}$
	10	40	55	150	2.73	$\frac{4}{3}$
	n	4n	$\frac{n(n+1)}{2}$	$n(n+5)$	$2+O(\frac{1}{n})$	$\frac{4}{3}$
50%	4	4	10	24	2.50	$\frac{1}{3}$
	7	7	28	63	2.25	$\frac{1}{3}$
	10	10	55	120	2.18	$\frac{1}{3}$
	n	n	$\frac{n(n+1)}{2}$	$n(n+2)$	$2+O(\frac{1}{n})$	$\frac{1}{3}$
0%	4	−8	10	12	1.2	$-\frac{2}{3}$
	7	−14	28	42	1.5	$-\frac{2}{3}$
	10	−20	55	90	1.64	$-\frac{2}{3}$
	n	−2n	$\frac{n(n+1)}{2}$	$n(n-1)$	$2+O(\frac{1}{n})$	$-\frac{2}{3}$

TABLE 2

Composition and Relevant Parameters of Triangular S-Edge Terminated Clusters as a Function of Sulfur Coverage

S coverage	Size	n_S	n_{Mo}^{tot}	n_S^{tot}	$\frac{n_S^{tot}}{n_{Mo}^{tot}}$	Δn_S
100%	4	10	10	30	3.00	$\frac{2}{3}$
	7	16	28	72	2.57	$\frac{2}{3}$
	10	22	55	132	2.40	$\frac{2}{3}$
	n	$2n+2$	$\frac{n(n+1)}{2}$	$n(n+3)+2$	$2+O(\frac{1}{n})$	$\frac{2}{3}$
50%	4	-2	10	18	1.80	$-\frac{1}{3}$
	7	-5	28	51	1.82	$-\frac{1}{3}$
	10	-8	55	102	1.85	$-\frac{1}{3}$
	n	$2-n$	$\frac{n(n+1)}{2}$	n^2+2	$2+O(\frac{1}{n})$	$-\frac{1}{3}$
0%	4	-14	10	6	0.60	$-\frac{4}{3}$
	7	-26	28	30	1.07	$-\frac{4}{3}$
	10	-38	55	72	1.31	$-\frac{4}{3}$
	n	$2-4n$	$\frac{n(n+1)}{2}$	$n(n-3)+2$	$2+O(\frac{1}{n})$	$-\frac{4}{3}$

For a triangular cluster of size n, we take into account the contribution of the corner energy, $\epsilon(\mu)$, and express the grand potential as the sum of the edge energy, $\sigma(\mu)$, times the number of edge atoms plus the corner energy times the number of corner atoms:

$$\Omega(n, \mu_S) = 3(n-1)\sigma(\mu_S) + 3\epsilon(\mu_S). \quad [7]$$

For large clusters, one can assume that σ and ϵ do not depend on n. According to Eq. [4], $\Omega(n, \mu_S = 0)$ can now be plotted as a function of n for the six different types of clusters, as shown in Fig. 4. The slopes of the fitted linear expression $3(n-1)\sigma(\mu_S = 0) + 3\epsilon(\mu_S = 0)$ yield values for the edge energies $\sigma(\mu_S = 0) = \sigma_0$ for each individual edge termination and for the corner energy $\epsilon(\mu_S = 0) = \epsilon_0$. It is important to emphasize that the calculated cluster energies lie in fact almost precisely on straight lines, validating expression [7], but small deviations are clearly visible. The reason for these deviations is that the stoichiometry changes with the cluster size, and in turn the filling of the electronic states at the edges varies. The observed deviations are therefore real finite-size effects.

The assumption of size-independent corner energies ϵ is violated in the case of the S-edge with 50% S coverage. When n is an odd number, frustration effects modify the corner site, which is in plane instead of following the zigzag structure. Treating systems with even and odd n independently leads to a linear relationship in both cases. The derived corner energies ϵ are different, but the surface energies σ are the same and can be deduced unambiguously.

At this stage we have determined the surface energy per edge atom, $\sigma(\mu_S = 0)$, and the corner energy, $\epsilon(\mu_S = 0)$, for *one particular* chemical potential, $\mu_S = 0$. To obtain the variation of the surface energy $\sigma(\mu_S)$ with respect to the chemical potential one can in principle repeat the procedure with a different chemical potential. It is however more straightforward to combine Eqs. [4], [6], and [7], yielding

$$\Omega(n+1, \mu_S) - \Omega(n, \mu_S) = 3\sigma(\mu_S) \quad [8]$$

and

$$\sigma(\mu_S) = \sigma_0 - \mu_S \Delta n_S, \quad [9]$$

where

$$\Delta n_S = \frac{n_S(n+1) - n_S(n)}{3}, \quad [10]$$

Δn_S does not depend on the size of the clusters, n, as shown in the Tables 1 and 2. The value Δn_S describes the slope of the edge energy $\sigma(\mu_S)$ with respect to the chemical potential of sulfur, but there is an even simpler interpretation for this number: it specifies the local stoichiometry of a surface site. $\Delta n_S = 0$ corresponds to a locally stoichiometric (nonpolar) surface area. Negative slopes correspond to excess sulfur, whereas positive slopes are related to sulfur deficiencies. In both cases the surface is formally polar.

Finally, to determine the equilibrium morphology, we use the Gibbs–Curie–Wulff construction (33), which states that

$$\frac{\sigma_{Mo}}{d_{Mo}} = \frac{\sigma_S}{d_S}, \quad [11]$$

where σ_{Mo} (σ_S) is the minimum of the surface energy

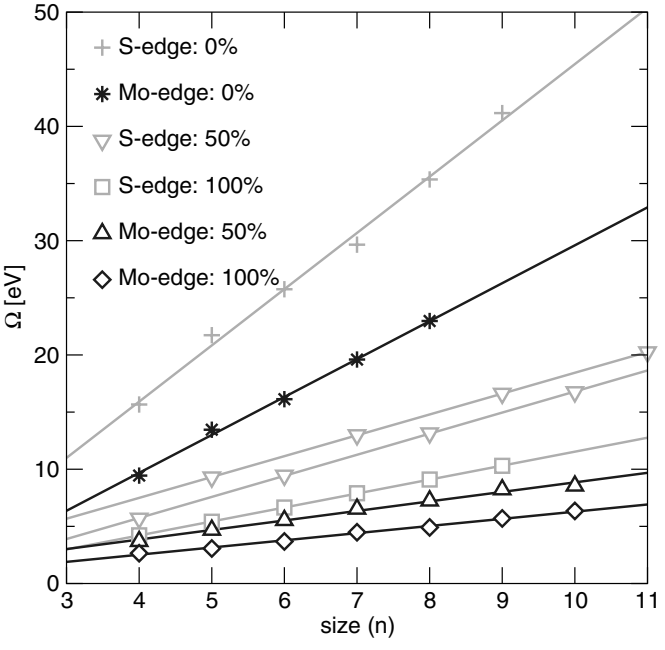

FIG. 4. Grand potential, Ω, as a function of the cluster size, n, for a chemical potential of sulfur equal to zero and for the two edges with various S coverages. The slopes of the straight lines represent σ_0. Note that two distinct lines are drawn for the S-edge with 50% S coverage, depending on the parity of n.

calculated using Eq. [9] for the Mo-edge (S-edge). d_{Mo} (d_S) stands for the distance of the Mo-edge (S-edge) to the center of mass of the particle.

In Eq. [4], we took as reference the infinite MoS_2 monolayer, which implies that σ_{Mo} and σ_S are determined independently from the surface energy of the basal plane. Furthermore, as the latter remains constant, whatever the edges may be, the cluster shape in two dimensions is determined by the ratio $\frac{\sigma_{Mo}}{\sigma_S}$. It can be shown that a ratio greater than 2 (smaller than 0.5) yields a triangle exhibiting the Mo-edge (S-edge) only. When this ratio is within the range of 0.5–2, the shape is a that of a deformed hexagon, with the percentage of the Mo-edges and S-edges given by their relative surface-energy values. The perfect hexagon is obtained for a ratio equal to 1. Finite-size effects (corner) energies have been neglected to this end, although they might be of significance for the small clusters observed, for instance, in the STM experiments. But our computational resources are yet not sufficient to determine required energies with sufficient accuracy.

D. Simulation of STM Images

Constant current STM topographs are simulated by calculating the energy-resolved charge density $\rho(\vec{r}, \epsilon)$ (50). We then evaluate iso-surfaces of constant charge density $\rho(\vec{r}, \epsilon) = C$ and determine the corrugation of these iso-surfaces. The constant C is chosen so that we typically scan at distances of 4 Å from the core of the outermost sulfur atoms. This approach has been successfully applied to oxides grown on a support (51) and to metallic surfaces (52). Within this approximation, there is no electronic interaction between the tip and the surface.

Although this approach is rather simplified, we are confident that the presented qualitative interpretations will be useful. More accurate but rather involved approaches were applied to simulate STM images of the MoS_2 basal plane (53–55), but to date no results have been reported for STM simulations of isolated MoS_2 triangles. The motivation for this part of the work is to shed light on the recent STM experiments of Helveg *et al.* (1), where MoS_2 nanoclusters were grown on Au(111).

In order to avoid electronic interactions between MoS_2 clusters belonging to two different cells, the size of the simulation boxes was increased to 10 Å in the direction perpendicular to the basal plane, and simultaneously the cutoff energy was raised to 325 eV. Since our present calculations are based on isolated clusters, which generally exhibit a rather large highest occupied molecular orbital (HOMO)–lowest unoccupied molecular orbital (LUMO) gap on the order of 0.5 eV, we are faced with deciding whether tunneling from the tip into the LUMO or tunneling from the HOMO into the tip should be simulated.

The position of the HOMO and LUMO, and the theoretical work function of Au, suggests that the LUMO of the MoS_2 clusters is located below the Fermi energy of Au. Hence, a fractional charge transfer from the Au slab to the cluster is expected, and the LUMO states of the unsupported cluster will become populated, as shown in (56) for periodic systems. It is therefore likely that the LUMO states are visualized in the STM experiments. Despite this we have decided to include both states, HOMO and LUMO, in our STM simulations. Typically states in an interval of roughly 0.1 eV around the HOMO and LUMO were taken into account (corresponding roughly to a bandwidth of 0.6 eV). Certainly this is the most significant approximation of the present STM simulations, and we would like to perform more accurate calculations taking into account the support in the future. But unfortunately such calculations are presently not possible, since our calculations have already approached the limits of current supercomputing facilities (200 Mo and S atoms; to model the support, roughly 200 additional Au atoms had to be used).

III. RESULTS AND DISCUSSION

A. Energetics and Morphologies

First of all, it should be noted that the following results are fully consistent with the ones obtained in Ref. (18). In particular, the stability domains with varying sulfur potential for an individual edge (S or Mo) agree with the results reported before. To achieve such consistent results, rather large clusters had to be used in order to obtain accurate extrapolations for the edge energies. The new insight brought by the present work concerns the simultaneous treatment of the Mo-edge and the S-edge. Previously, we could only determine how the sulfur coverage varied for the Mo-edge, for example, when the partial sulfur pressure was changed. Now we can determine the relative stability of the S- and Mo-edges and hence decide whether the S-edge or the Mo-edge is energetically favorable.

The surface energy $\sigma(\mu_S)$ as a function of the chemical potential of sulfur, μ_S, is reported in Fig. 5 for the six investigated edges. Each straight line corresponds to one type of edge with a given sulfur coverage. The slope of the straight lines is given by the value of Δn_S and the ordinate at the origin by σ_0 (Eq. [9]). In this type of diagram, the most stable edge is always the one with the lowest energy, and clearly the stable edge changes with the chemical potential μ_S. As emphasized before, μ_S is controlled by the experimental conditions. As described by Eq. [2], strongly sulfiding conditions correspond to the right-hand-side of the diagram (high H_2S partial pressures), whereas strongly reducing conditions are found at the left-hand-side (large H_2 partial pressure). A typical value of μ_S for HDS working conditions ($T = 650$ K, $p_{H_2S}/p_{H_2} = 0.01$) is -1 eV. The grey-shaded region at the left of Fig. 5 represents the chemical potential domain where the MoS_2 bulk phase is reduced into bcc Mo and H_2S.

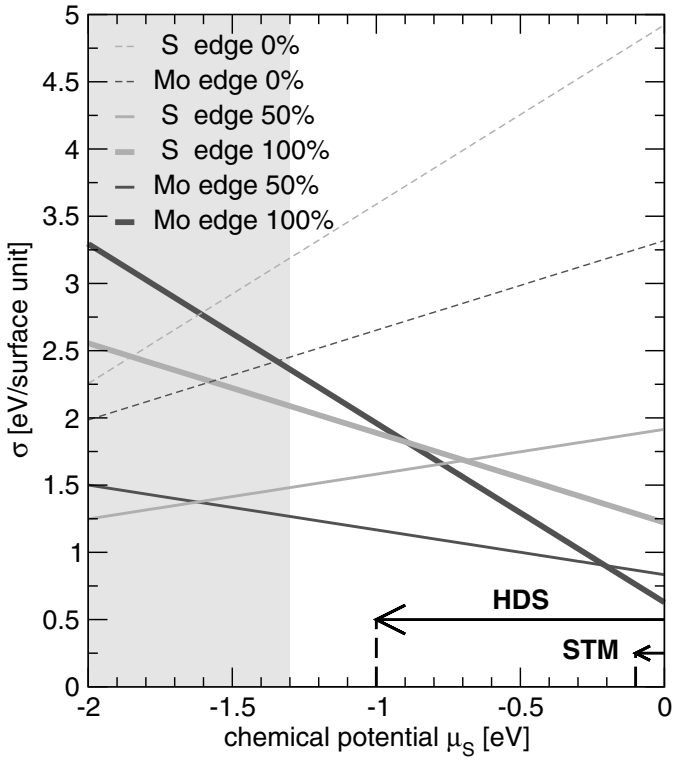

FIG. 5. Variation of the surface energy as a function of chemical potential of sulfur. Realistic HDS working conditions and STM conditions are represented by arrows (see text for explanations). MoS_2 is unstable in the grey-shaded region.

For $\mu_S = 0$, the Mo-edge covered by 100% sulfur results in the lowest surface energy ($\sigma_0 = 0.65$ eV). This demonstrates that at strong sulfiding conditions the Mo-edge is terminated by sulfur dimers, as shown in Fig. 2a. Under these conditions, the S-edge would be covered by 100% sulfur atoms as well, exhibiting the local structure depicted by Fig. 3a. However, its surface energy is about 1.25 eV, which is significantly larger than that of the Mo-edge.

Decreasing the chemical potential of sulfur at fixed temperature T corresponds to either decreasing p_{H_2S} or increasing p_{H_2}. For μ_S smaller than -0.2 eV, a crossover between the Mo-edge covered by 100% S atoms and the Mo-edge covered by 50% S atoms occurs. The surface energy of the stable Mo-edge remains smaller than that of the S-edge as long as μ_S is greater than -1.65 eV. For $\mu_S < -1.65$ eV, the relative stability between the Mo-edge with 50% S coverage and the S-edge with 50% S coverage starts to favor the latter. However, this chemical potential is beyond the limit of stability of MoS_2 particles, estimated to be around -1.30 eV. This shows that for all relevant conditions the Mo-edge is in fact energetically significantly more stable than the S-edge, and hence under any realistic conditions, the Mo-edge will be more abundant than the S-edge.

The competition between the Mo and S terminated edges is represented in Fig. 6, where the relative amount of Mo-edge with respect to the total circumference is plotted. This diagram is a direct transcription of the Gibbs–Curie–Wulff relationship (Eq. [11]), and it shows the morphology of the MoS_2 particles as a function of the chemical potential. To derive this type of diagram, we simply deduced the energies of the most stable reconstructions of the S- and Mo-edges from Fig. 5 for each chemical potential, μ_S, and then applied Eq. [11].

The key result of this diagram is that the morphology itself can be modified by the sulfiding conditions. At high chemical potential ($\mu_S > -0.6$ eV), about 80–90% of the entire circumference exhibits Mo-edges. The nanoparticles will have the shape of capped or corner truncated triangles, exposing Mo-edges on the long sides and a small area of S-edges at the corners, where the triangle is capped. The composition of the Mo-edge changes with the chemical potential of sulfur, as discussed before, and this is again visible in Fig. 6 (change from Mo 100% to Mo 50% at -0.2 eV). The composition of the S-edge also changes from 100% S coverage to 50% coverage at $\mu_S = -0.55$ eV. For the conditions used to synthesize the MoS_2 particles that were investigated in the STM study (1) the temperature was fixed at 400 K and the sulfiding conditions are pure H_2S. In this case, the chemical potential is relatively high (close to 0 eV), and as a consequence, the area of the Mo-edge represents about 85–90% of the circumference.

For the nanoparticles observed in the STM with roughly 13 Mo atoms at the long Mo-edge ($n \approx 13$), the length of the S-edge should correspond to roughly one or two lattice constants (see Fig. 6b). This is almost what is observed in the experiment. One must keep in mind that the Gibbs–Curie–Wulff construction is only correct in the macroscopic limit, when corner energies can be neglected. The slight disagreement, therefore, does not necessarily point to any deficiencies in the present calculations.

For smaller μ_S, the S-edge area keeps increasing up to the MoS_2 stability limit. As a consequence, although perfect MoS_2 hexagons are very unlikely to be formed under realistic sulfiding conditions, deformed hexagons should be observable experimentally. Indeed, for typical sulfiding reaction conditions ($T = 350$ K, and $\frac{p_{H_2S}}{p_{H_2}} \simeq 0.05$), μ_S is close to -1 eV and the shape of MoS_2 particles should exhibit mostly Mo-edges with a single bridging sulfur atom (60% area) and about 40% S-edges exposing S atoms in a zigzag configuration, such as depicted in Fig. 6c.

B. STM Images

STM images are simulated for four relevant triangular-shaped clusters with the largest sizes ($n = 9$ or 10) accessible to our calculations. For the S-edge (Mo-edge) model covered by 100 and 50% S atoms (Mo atoms) the results are reported in Fig. 7 (Fig. 8). The underestimation of the charge density in the center of the cluster is attributed to the fact that we neglect the interaction with the gold support

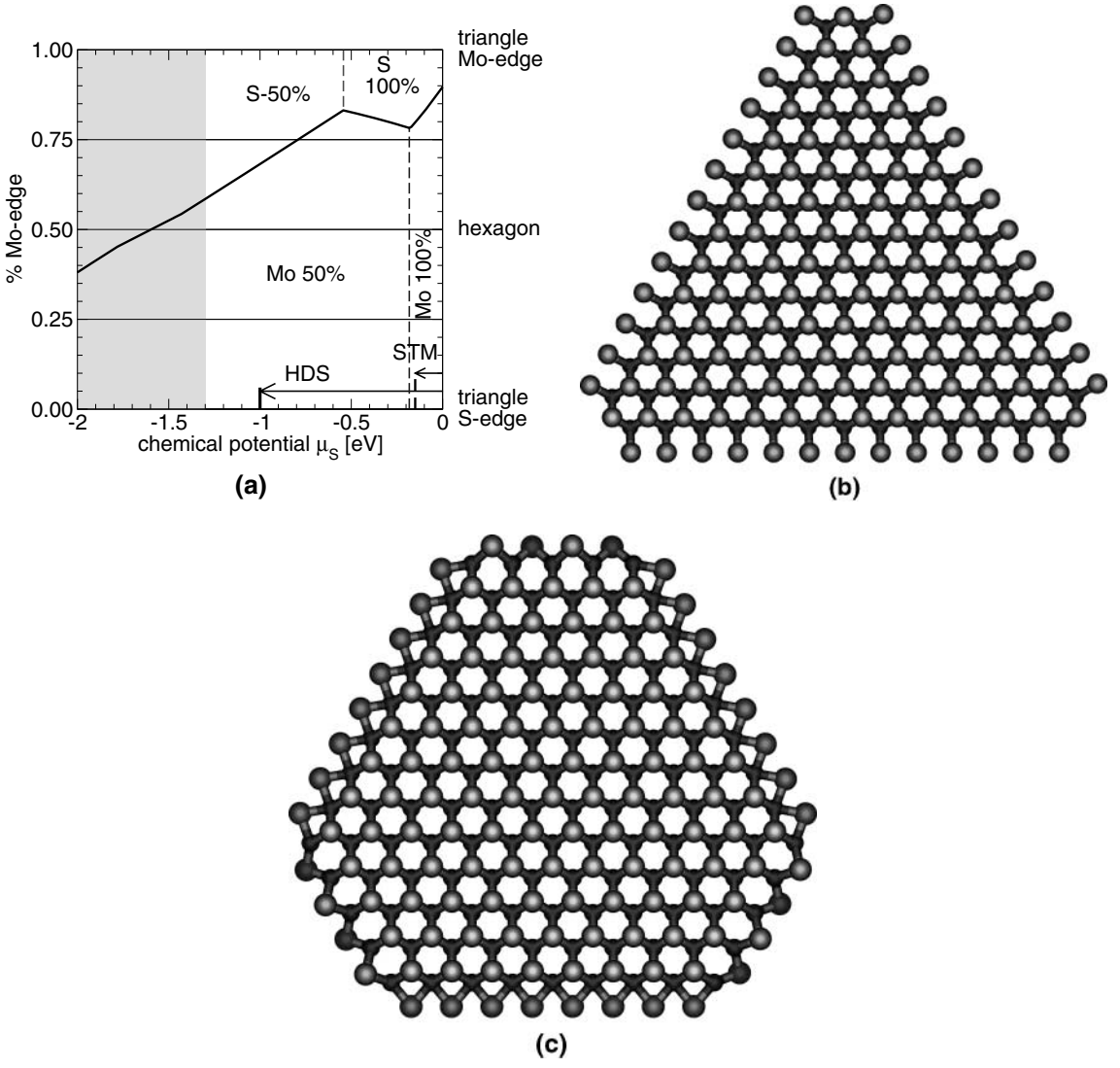

FIG. 6. (a) Morphology of the MoS_2 nanosize particles as a function of chemical potential of sulfur. The ordinate represents the percentage of Mo-edge. For 100% (0%) Mo-edge, the shape is a perfect Mo-edge (S-edge) triangle. For 50% Mo-edge, the particle is a perfect hexagon. The thick line indicates the equilibrium morphology. (b, c) The two clusters correspond to (b) STM conditions and (c) HDS working conditions.

[see Section IID and Ref. (56)]. Despite this discrepancy, some of the STM images are obviously very similar to the experimental STM data, enabling the following analysis.

The most striking and common feature of all models is a bright rim on the triangle's periphery. In the case of S-edge with 100% S, the bright rim is found above the outermost S atoms (Fig. 7a), whereas in all other cases, it is above the second row of S atoms (Figs. 7b and 8). This rim derives from a surface state which is localized on these S atoms. The bright spots or protusions observed at the edge of Figs. 7b and 8 exhibit a significantly weaker intensity. This is a simple geometric effect, since in all cases but the S-edge triangle with 100% S coverage, the outermost S atoms are not located in the same plane as the S atoms in the center of the triangle (see Figs. 2a, 2b, and 3b).

Let us first concentrate on the two triangles exposing the S-edge. As already emphasized these surfaces are energetically not favorable at realistic conditions. In the STM, the protrusions at the edge are clearly localized above the position of the S atoms, which are indicated by large circles. For the S-edge covered with a 100% S coverage, the protrusions at the edges and the bright rim are merging. For the S-edge covered by 50% S atoms, the intensity at every second S atom is larger, which is again a simple geometrical effect: the S atoms form a zigzag chain at the edge (Fig. 3b). Clearly none of these two models resembles the experimentally observed STM images, since in the experimental STM the protrusions at the edges are not in the registry of the S atoms from the center of the cluster. Therefore, we can rule out the possibility that any two of these models

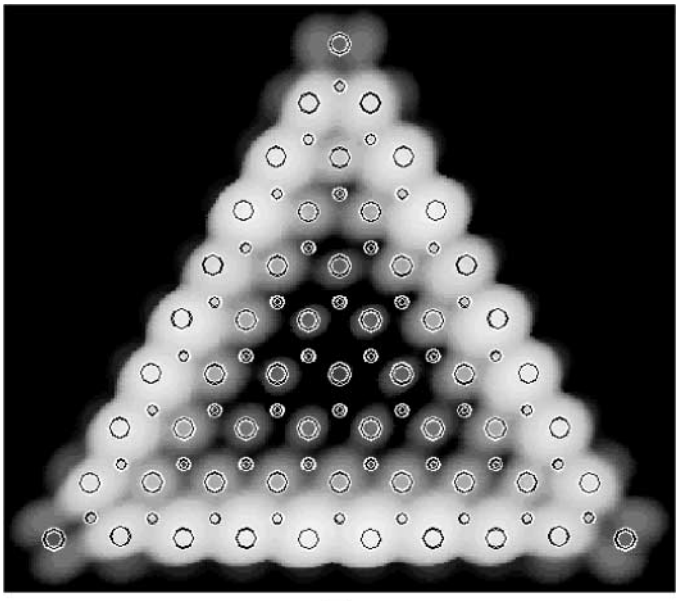

(a)

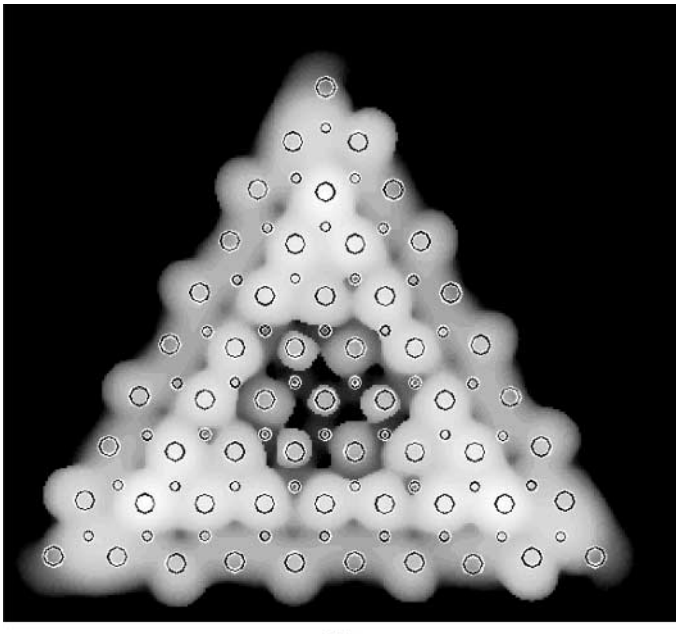

(b)

FIG. 7. Simulated STM image for the S-edge covered by (a) 100% S atoms and (b) 50% S atoms. Large circle, sulfur atoms; small circles, molybdenum atoms. The corresponding local structures are represented in Figs. 3a and 3b, respectively.

correspond to the experimentally observed triangles (1). This fully confirms the energetic arguments applied in the previous section.

We now focus on the two models predicted to be thermodynamically stable: the Mo-edge with 100% sulfur coverage, and the Mo-edge with 50% sulfur coverage. The bright rim close to the second S atom was already discussed. Additionally, in both cases, a significant intensity enhancement appears on the corners of the triangular clusters in the simulated images. Third, the protrusions at the edges exhibit a lower intensity than the bright rim. All three observations are in agreement with the experiment. Fourth and most important, in both cases, the protrusions at the edge are located out of the registry with respect to the sulfur atoms in the center of the triangles.

The origin of this phenomenon is different in both cases. For the edge terminated with a single S atom, the S atom itself is located out of the registry and is seen as a protrusion in the simulated STM. For the edge terminated with two S atoms, the protrusions are, however, located between the S atoms. The protrusion arises from a surface state with σ_p character, as discussed in Ref. (56). We, however, observe one feature not seen in Ref. (56). The S_2 dimers have a slight tendency to pair (see Section IIB). Although the effect is geometrically very small, it clearly leads to a similar bright–dark alternation at the edge, as observed in the experiment. However this alternation, which is not observed in periodic calculations, as discussed in (18), depends also on the parity of n. Any proposed explanation must be found in the effects attributable to stoichiometry as well as to corners modifying the Fermi level in the finite-size system.

The conclusion of this section is that the STM images for the Mo-edge with 100 and 50% S coverage are quite similar, as far as the positions of the protrusions at the edge is concerned; for both cases, the protrusions at the edge are not in the same registry as the S atoms in the center of the cluster. The Mo-edge with 100% S coverage shows better quantitative agreement with the experiment; it reproduces in particular the period of two observed in the experiment. But we remark that recent pictures for the Co-activated MoS_2 catalyst shows edges without an additional periodicity of 2, as reported in Ref. (29). It is our impression that these images are in fact very similar to the STM simulation of the Mo-edge with 50% S coverage. Generally, the qualitative similarity of both images shows that a straightforward distinction between the two reconstructions is difficult on the basis of experimental STM images alone.

C. *Effect of Vacancy Creation*

In this section, we investigate whether the partial pressure of hydrogen under HDS reaction conditions may allow the creation of local defects on MoS_2 nanoparticles. We concentrate mainly on the Mo-edge with a bridging S atom (50% S), since this is the stable edge at the relevant HDS conditions. The energy required to remove a single S atom from the middle of the edge varies with the cluster size. It is yet not fully converged for the clusters investigated here, but it seems to settle at around 1 eV for $n > 8$. For periodic calculations, we previously reported a value

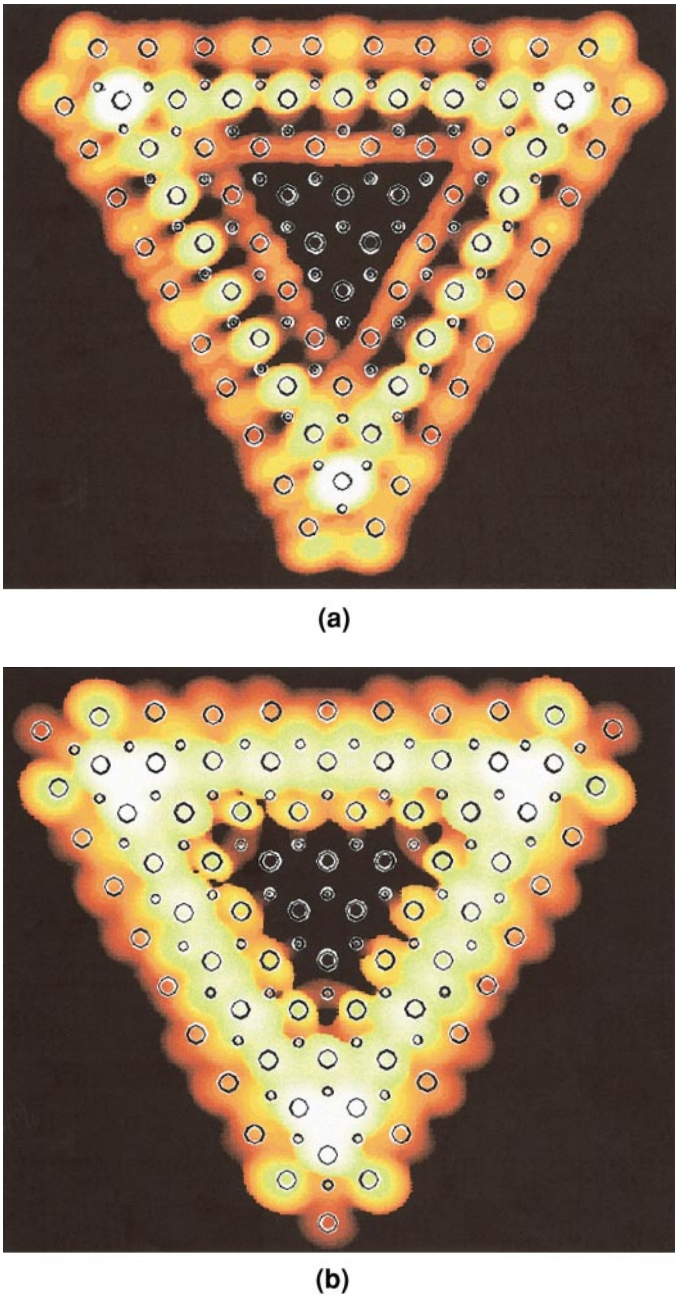

FIG. 8. Simulated STM image for the Mo-edge covered by (a) 100% S coverage and (b) 50% S atoms. The corresponding local structures are represented in Figs. 2a and 2b, respectively.

of 1.26 eV, in reasonable agreement with the present value considering that the latter value corresponded to the rather high vacancy concentration of 33% (18).

We plot in Fig. 9 the grand canonical potential for a cluster of size $n = 9$ as a function of μ_S, such as it is given by Eq. [4] and including the presence of one vacancy either at every edge or at every corner. The diagram of Fig. 9 shows only the most representative edge structures. The crossover between the straight lines of the Mo-edge with 50% S coverage and the same edge with one vacancy within the edge occurs at $\mu_S \simeq -1$ eV. This result demonstrates clearly that a S vacancy on the edge can be reached under HDS working conditions.

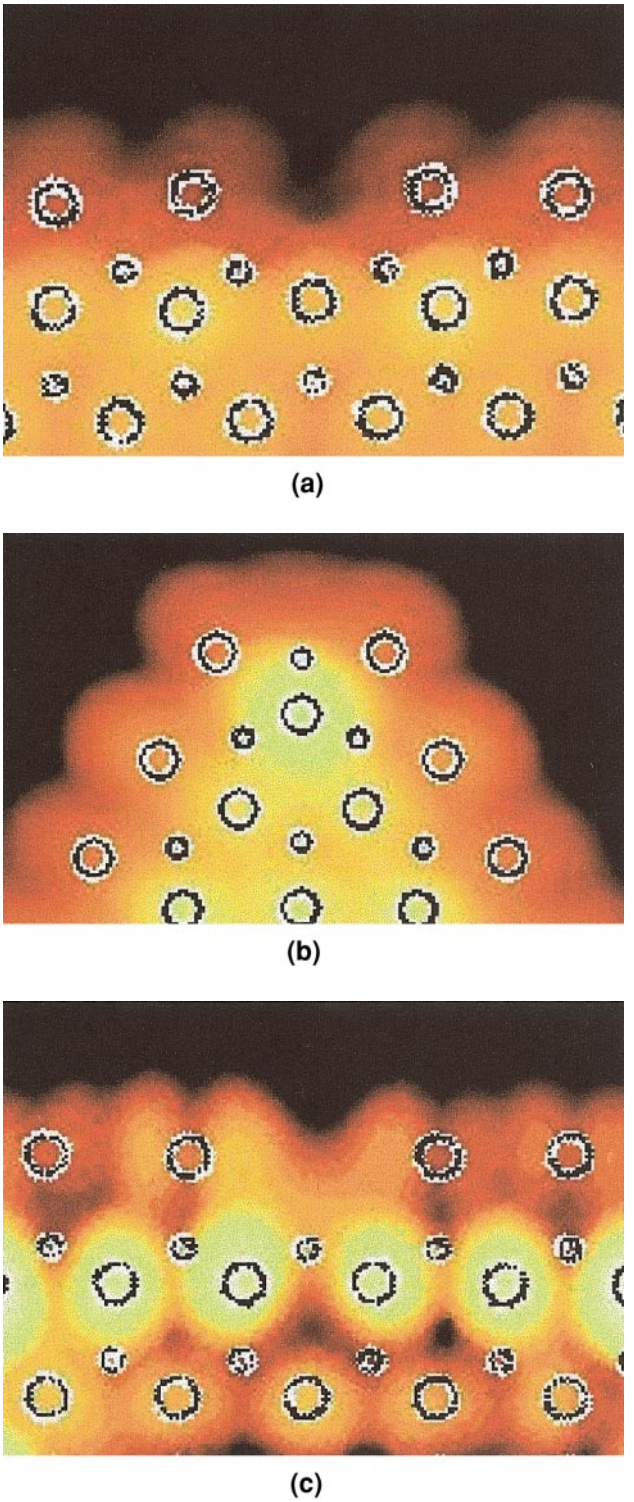

FIG. 10. STM images of triangular clusters with (a) one S-bridging removal at the Mo-edge, (b) one vacancy on the corner, and (c) one S_2 dimer removal at the Mo-edge.

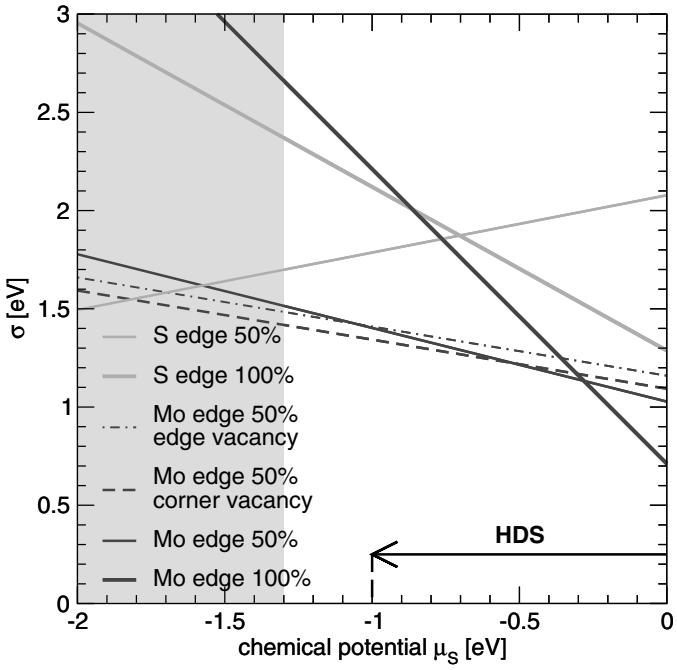

FIG. 9. Thermodynamic stability of clusters ($n = 9$) with S vacancies on the edge and at the corner as a function of the chemical potential of sulfur. Typical HDS working condition is represented by the arrow.

However, the striking result is that even less energy is required to create a vacancy at the corner. The vacancy formation energy for such a defect seems to approach a value of 0.5 eV. Thus, for $\mu_S < -0.5$ eV the corner will expose a coordinatively unsaturated Mo site, which indicates that corner vacancies might play a key role in the reactivity of MoS_2 clusters. Figures 10a and 10b represent the STM image simulated for the two possible scenarios. Figure 10a is again in qualitatively good agreement with the experimental image, which was taken after exposing the MoS_2 particle to reactive H atoms (1). The protrusion over the removed S bridging atom has, as a matter of fact, vanished. Simultaneously, the bright spot localized on the S atom of the first S sublayer has slightly decreased in intensity. To make our study complete, we report, in Figure 10c, the simulated STM image for Mo-edge (initially covered by 100% S atoms) after removal of one S dimer. Again, a depletion is observed in the region where the dimer has been removed, whereas a slight enhancement appears around the vacant position. Removing such a dimer from the edge should take place at $\mu_S \simeq -1$ eV, where the Mo-edge with 50% S coverage is already more stable.

IV. CONCLUSIONS

We have calculated accurate surface energies for the individual edges of MoS_2 single-layer sheets using large-cluster models. In contrast to slab calculations, where only the average of the surface energies of the Mo-edge and S-edge can be obtained, triangles allow for an accurate determination of the surface energy of each individual edge. We demonstrate that the Mo-edge is energetically the most stable surface under realistic HDS or working conditions. Combination of these surface energies with the Gibbs–Curie–Wulff construction shows that the shape is controlled by the working conditions.

At very high presure of H_2S, our calculations predict that almost perfectly triangular-shaped particles are expected to grow, exposing mostly Mo-edges. This agrees well with the triangles observed in the STM experiment. As far as the termination of the edges in the experimentally observed clusters is concerned, our study also shows that the Mo-edge termination changes with the chemical potential of sulfur from 100% sulfur to 50% sulfur in the region where the MoS_2 particles are grown in the experiment. The STM simulations cannot rule out one of the two terminations, since the images for the 100 and 50% sulfur-terminated Mo-edge are fairly similar. In fact, we think that both terminations might be observed at different experimental conditions.

With respect to catalysis, it is, however, more important to predict which morphology and edge sites the nanoparticles will expose under realistic HDS conditions. Our study demonstrates clearly that deformed hexagons exhibiting roughly 60% of the Mo-edge and 40% of the S-edge are thermodynamically stable. We have also addressed the creation of vacancies for such clusters and found that the formation of vacancies is thermodynamically possible. It is interesting that sulfur removal from corners is much easier ($\mu_S = -0.5$ eV) than from edges ($\mu_S = -1$ eV). This suggests that corners might play a key role in catalytic properties of nonpromoted MoS_2 particles.

In future work, the promoting effect by 3d transition metals (Co or Ni) should be investigated. Previous DFT calculations (19) enabled detailed determination of the local structure of such systems. Indeed, the promoter acting as surfactant may induce further shape modifications, by changing significantly the surface energies, as suggested in Ref. (31).

ACKNOWLEDGMENTS

This work has been performed within the Groupement de Recherche Européen *Dynamique Moléculaire Quantique Appliquée à la Catalyse*, a joint project of the Conseil National de la Recherche Scientifique (CNRS), Institut Français du Pétrole (IFP), Universität Wien, Total Fina Elf, and Eindhoven University. Work at Universität Wien has been supported by the Institut Français du Pétrole (IFP).

REFERENCES

1. Helveg, S., Lauritsen, J. V., Lægsgaard, E., Stensgaard, I., Clausen, B. S., Topsøe, H., and Besenbacher, F., *Phys. Rev. Lett.* **84**, 951 (2000).
2. Topsøe, H., Clausen, B. S., and Massoth, F. E., *in* "Hydrotreating Catalysis and Science and Technology" (J. R. Anderson and M. Boudart, eds.), Vol. 11, p. 29. Springer-Verlag, Berlin/Heidelberg, 1996.

3. Prins, R., in "Handbook of Heterogeneous Catalysis" (G. Ertl, H. Knözinger, and J. Weitkam, Eds.), p. 1908. VHC, Weinheim, 1997.
4. Delannay, F., *Appl. Catal.* **16**, 135 (1985).
5. Payen, E., Kasztelan, S., Houssenbay, S., Szymanski, R., and Grimblot, J., *J. Phys. Chem.* **93**, 6501 (1989).
6. Alstrup, I., Chorkendorff, I., Candia, R., Clausen, B. S., and Topsøe, H., *J. Catal.* **77**, 397 (1982).
7. Kasztelan, S., Grimblot, J., Bonnelle, J. P., Payen, E., Toulhoat, H., and Jacquin, Y., *Appl. Catal.* **7**, 91 (1983).
8. Garreau, F. B., Toulhoat, H., Kasztelan, S., and Paulus, R., *Polyhedron* **5**, 211 (1986).
9. Houssenbay, S., Kasztelan, S., Toulhoat, H., Bonnelle, J. P., and Grimblot, J., *J. Phys. Chem.* **93**, 7176 (1989).
10. Wivel, J., Candia, R., Clausen, B., Mørup, S., and Topsøe, H., *J. Catal.* **68**, 453 (1981).
11. Payen, E., Kasztelan, S., and Grimblot, J., *J. Mol. Struct.* **71**, 174 (1988).
12. Chianelli, R. R., Ruppert, A. F., Jose-Yacamán, M., and Vázquez-Zavala, A., *Catal. Today* **23**, 269 (1995).
13. Clausen, B. S., Topsøe, H., Candia, R., Villadsen, J., Lengeler, B., Als-Nielsen, J., and Christensen, F., *J. Phys. Chem.* **85**, 3868 (1981).
14. Clausen, B. S., and Topsøe, H., *Hyperfine Interact.* **47**, 203 (1989).
15. Bouwens, S. M. A. M., Prins, R., de Beer, V. H. J., and Koningsberger, D. C., *J. Phys. Chem.* **94**, 3711 (1990).
16. Calais, C., Matsubayashi, N., Geantet, C., Yoshimura, Y., Shinada, H., Nishijima, A., Lacroix, M., and Breysse, M., *J. Catal.* **174**, 130 (1998).
17. Shido, T., and Prins, R., *J. Phys. Chem.* **102**, 8426 (1998).
18. Raybaud, P., Hafner, J., Kresse, G., Kasztelan, S., and Toulhoat, H., *J. Catal.* **189**, 129 (2000).
19. Raybaud, P., Hafner, J., Kresse, G., Kasztelan, S., and Toulhoat, H., *J. Catal.* **190**, 128 (2000).
20. Byskov, L. S., Hammer, B., Norskov, J. K., Clausen, B. S., and Topsøe, H., *Catal. Lett.* **47**, 177 (1997).
21. Byskov, L. S., Norskov, J. K., Clausen, B. S., and Topsøe, H., *J. Catal.* **187**, 109 (1999).
22. Raybaud, P., Hafner, J., Kresse, G., and Toulhoat, H., *J. Phys. Condens. Matter* **9**, 11085 (1997).
23. Raybaud, P., Hafner, J., Kresse, G., and Toulhoat, H., *J. Phys. Condens. Matter* **9**, 11107 (1997).
24. Toulhoat, H., Raybaud, P., Kasztelan, S., Kresse, G., and Hafner, J., *Catal. Today* **50**, 629 (1999).
25. Raybaud, P., Hafner, J., Kresse, G., and Toulhoat, H., *Phys. Rev. Lett.* **80**, 1481 (1998).
26. Raybaud, P., Hafner, J., Kresse, G., Kasztelan, S., and Toulhoat, H., *Stud. Surf. Sci. Catal.* **127**, 309 (1999).
27. Cristol, S., Paul, J. F., Payen, E., Bougeard, D., Hafner, J., and Hutschka, F., *Stud. Surf. Sci. Catal.* **127**, 327 (1999).
28. Raybaud, P., Digne, M., Iftimie, R., Wellens, W., Euzen, P., and Toulhoat, H., *J. Catal.* **201**, 236 (2001).
29. Lauritsen, J. V., Helveg, S., Lægsgaard, E., Stensgaard, I., Clausen, B. S., Topsøe, H., and Besenbacher, F., *J. Catal.* **197**, 1 (2001).
30. Kasztelan, S., Toulhoat, H., Grimblot, J., and Bonnelle, J., *Appl. Catal.* **13**, 127 (1984).
31. Toulhoat, H., and Kasztelan, S., *in* "Proceedings, 9th International Congress on Catalysis, Calgary, 1988" (M. J. Phillips and M. Ternan, Eds.), p. 31. Chem. Institute of Canada, Ottawa, 1988.
32. Kasztelan, S., *Langmuir* **6**, 590 (1990).
33. Wulff, G., *Z. Kristallogr.* **34**, 449 (1901).
34. Herring, C., *Phys. Rev.* **82**, 87 (1951).
35. Hohenberg, P., and Kohn, W., *Phys. Rev. B* **136**, 864 (1964).
36. Kohn, W., and Sham, L. J., *Phys. Rev. A* **140**, 1133 (1965).
37. Jones, R. O., and Gunnarsson, O., *Rev. Mod. Phys.* **61**, 689 (1989).
38. Car, R., and Parrinello, M., *Phys. Rev. Lett.* **55**, 2471 (1985).
39. Payne, M. C., Teter, M. P., Allan, D. C., Arias, T. A., and Joannopoulos, J. D., *Rev. Mod. Phys.* **64**, 1045 (1992).
40. Kresse, G., and Hafner, J., *Phys. Rev. B* **47** (588), 14251 (1993).
41. Kresse, G., and Furthmüller, J., *Computat. Mater. Sci.* **6**, 15 (1996).
42. Blöchl, P. E., *Phys. Rev. B* **50**, 17953 (1994).
43. Vanderbilt, D., *Phys. Rev. B* **41**, 7892 (1990).
44. Kresse, G., and Hafner, J., *Phys. Rev. B* **49**, 14251 (1994).
45. Kresse, G., and Joubert, D., *Phys. Rev. B* **59**, 1758 (1999).
46. Raybaud, P., Hafner, J., Kresse, G., and Toulhoat, H., *Surf. Sci.* **407** (237) (1998).
47. Perdew, J. P., and Zunger, A., *Phys. Rev.* **B 23**, 5084 (1987).
48. Perdew, J. P., Chevary, J. A., Vosko, S. H., Jackson, K. A., Pedersen, M. R., Singh, D. J., and Fiolhais, C., *Phys. Rev. B* **46**, 6671 (1992).
49. Perdew, J. P., and Wang, Y., *Phys. Rev. B* **45**, 13244 (1992).
50. Tersoff, J., and Hamann, D. R., *Phys. Rev. B* **31**, 805 (1985).
51. Surnev, S., Vitali, L., Ramsey, M. G., Netzer, F. P., Kresse, G., and Hafner, J., *Phys. Rev. B* **61**, 13945 (2000).
52. Eichler, A., Mittendorfer, F., and Hafner, J., *Phys. Rev. B* **62**, 4744 (2000).
53. Fisher, A. J., and Blöchl, P. E., *Phys. Rev. Lett.* **70**, 3263 (1993).
54. Kobayashi, K., and Yamauchi, J., *Phys. Rev. B* **51**, 17085 (1995).
55. Altibelli, A., Joachim, C., and Sautet, P., *Surf. Sci.* **367**, 209 (1996).
56. Bollinger, M. V., Jacobsen, K. W., Norskov, J. K., Lauritsen, J. V., Helveg, S., and Besenbacher, F., *Phys. Rev. Lett.* **87** (19), 6803 (2001).